Catalysis Science & Technology

ROYAL SOCIETY OF CHEMISTRY

PAPER

View Article Online
View Journal | View Issue

Cite this: *Catal. Sci. Technol.*, 2021, 11, 943

Amorphous Co_3S_4 nanoparticle-modified tubular g-C_3N_4 forms step-scheme heterojunctions for photocatalytic hydrogen production†

Yuanpeng Wang,[abc] Xuqiang Hao,[abc] Lijun Zhang,[abc] Zhiliang Jin *[abcd] and Tiansheng Zhao *[d]

Received 13th October 2020,
Accepted 18th November 2020

DOI: 10.1039/d0cy02009e

rsc.li/catalysis

An effective method to reduce the recombination rate of photogenerated electron–hole pairs was developed by the construction of heterojunctions with rationally designed photocatalysts having a matched band structure. Herein, g-C_3N_4 hexagonal tubes possessing a lower conduction band were coupled with Co_3S_4 ultra-fine nanoparticles having relatively higher positions for their conduction band. A step-scheme heterojunction was constructed between these two materials, and through this heterojunction, the spatial charge separation was boosted. The boosted spatial charge separation led to more useful electrons with a higher reduction ability that participated in a photocatalytic H_2 evolution reaction. The Co_3S_4 ultra-fine nanoparticles act as a mirror to repeatedly scatter and reflect incident light and thus enhance light utilization, and they also accelerate the spatial charge separation. The photocatalytic H_2 evolution activity of the composite catalyst reached 2120 μmol g^{-1} h^{-1}, which was 176 times higher than that of pristine g-C_3N_4 tubes. A series of characteristics were determined to investigate the interaction that occurred between the g-C_3N_4 hexagonal tubes and the Co_3S_4 ultra-fine nanoparticles, and to study the mechanism of the formed step-scheme. This work will guide the design of step-scheme heterojunction-based photocatalysts to produce H_2 from photocatalytic water splitting.

1. Introduction

The energy shortage and crisis have severely restricted sustainable development. Hydrogen (H_2) is a clean and environmentally friendly energy that can be produced from photocatalytic water splitting using inexhaustible solar energy, and hydrogen has been regarded as a promising renewable energy to meet the energy shortage and crisis.[1,2] Therefore, there has been an intense effort to discover an inexpensive, stable, and robust photocatalyst. Many photocatalysts such as metal-contained catalysts[3–14] and graphdiyne (GD)[15–17] or new members of carbon families or other metal-free catalysts[18] have been widely researched. g-C_3N_4 is a new member of photocatalysts that is metal-free and shows great prospect in practical applications because it was first applied to produce H_2 from water splitting by photocatalysis.[19] Even though it possesses high thermal and chemical stability and it is a metal-free photocatalyst that can be easily obtained, bulk g-C_3N_4 is subjected to intrinsic drawbacks, such as low specific surface area, and severe recombination of photo-generated electron–hole pairs.[20,21] Therefore, ongoing efforts have been devoted to solve these problems by resolving the deficiencies of bulk g-C_3N_4. Acquiring unique morphology and structure by adjusting synthetic methodologies will increase the specific surface area or make some adjustment to the band structure of g-C_3N_4 and increase the transfer efficiency of electron–holes in g-C_3N_4. Thus far, a host of different morphologies of g-C_3N_4, such as nanorods,[22] seaweeds,[23] nanosheets[24] and tubular g-C_3N_4 (ref. 25–28) have been rationally designed to increase the light harvesting ability of g-C_3N_4 or to adjust its band structure to overcome the intrinsic drawbacks of bulk g-C_3N_4. Surprisingly, results can be obtained by constructing a certain morphology of photocatalysts. For instance, g-C_3N_4 with a nanotube shape can contribute a large specific surface area to provide a large number of active sites, and it also shortens the transfer distance of photo-induced carriers in g-C_3N_4 from

[a] *School of Chemistry and Chemical Engineering, North Minzu University, Yinchuan 750021, P.R. China. E-mail: zl-jin@nun.edu.cn*
[b] *Ningxia Key Laboratory of Solar Chemical Conversion Technology, North Minzu University, Yinchuan 750021, P.R. China*
[c] *Key Laboratory for Chemical Engineering and Technology, State Ethnic Affairs Commission, North Minzu University, Yinchuan 750021, P.R. China*
[d] *State Key Laboratory of High-efficiency Utilization of Coal and Green Chemical Engineering, Ningxia University, Yinchuan, 750021, P.R. China.*
E-mail: zhaots@nxu.edu.cn

† Electronic supplementary information (ESI) available. See DOI: 10.1039/d0cy02009e

the phase to its surface. In addition, tubular g-C_3N_4 with a hollow structure can enhance light absorption and increase the separation and transfer kinetics of photo-generated charge carriers by the multiple light scattering/reflection effect in the inner cavity of g-C_3N_4.

Even though the different morphologies of g-C_3N_4 are rationally designed and all of them exhibit increased photocatalytic performance, the synthesis methods are time-consuming, expensive, and require hazardous reagents that are harmful to environment in the process of removing the template. Certain structured micro- or nano-materials are designed and obtained by treating supermolecular precursors that self-assemble through hydrogen bonding among molecules, and these materials are applied to many fields such as photocatalysis because the hydrogen bonding possesses features of strong direction and saturation.[29,30] It is well known that using water as the solvent in the process of synthesis is more beneficial for the self-assembly of molecules based on hydrogen bonding because they can acquire precursors that are stable and large. Additionally, there are quite a few advantages such as inexpensive, easily obtained, and environmentally friendly when choosing water as the solvent to obtain supermolecular precursors.

In this work, g-C_3N_4 with a tubular shape was fabricated by choosing deionized water as the solvent to synthesize supermolecular precursors and then calcine the precursors. Then, ultrafine Co_3S_4 nanoparticles were anchored on the surface of tubular g-C_3N_4 as cocatalyst to enhance the photocatalytic performance of g-C_3N_4. The results of emission scanning electron microscopy and transmission electron microscopy showed that the supermolecular precursors derived from melamine formed hollow g-C_3N_4 tubes, and ultrafine Co_3S_4 nanoparticles were distributed on the surface of the g-C_3N_4 tubes. The hollow structure enhances the light absorbed by g-C_3N_4, which is beneficial for the multiple light scattering/reflection effect in the inner cavity of g-C_3N_4. Even though the multiple light scattering/reflection effect in the inner cavity of g-C_3N_4 enhances its light absorption, light utilization is still inefficient in the outward wall because light entering into the tube can be utilized on both tails of the tube. The ultrafine Co_3S_4 nanoparticles distributed on the surface of the tube alter the relatively smooth surface of g-

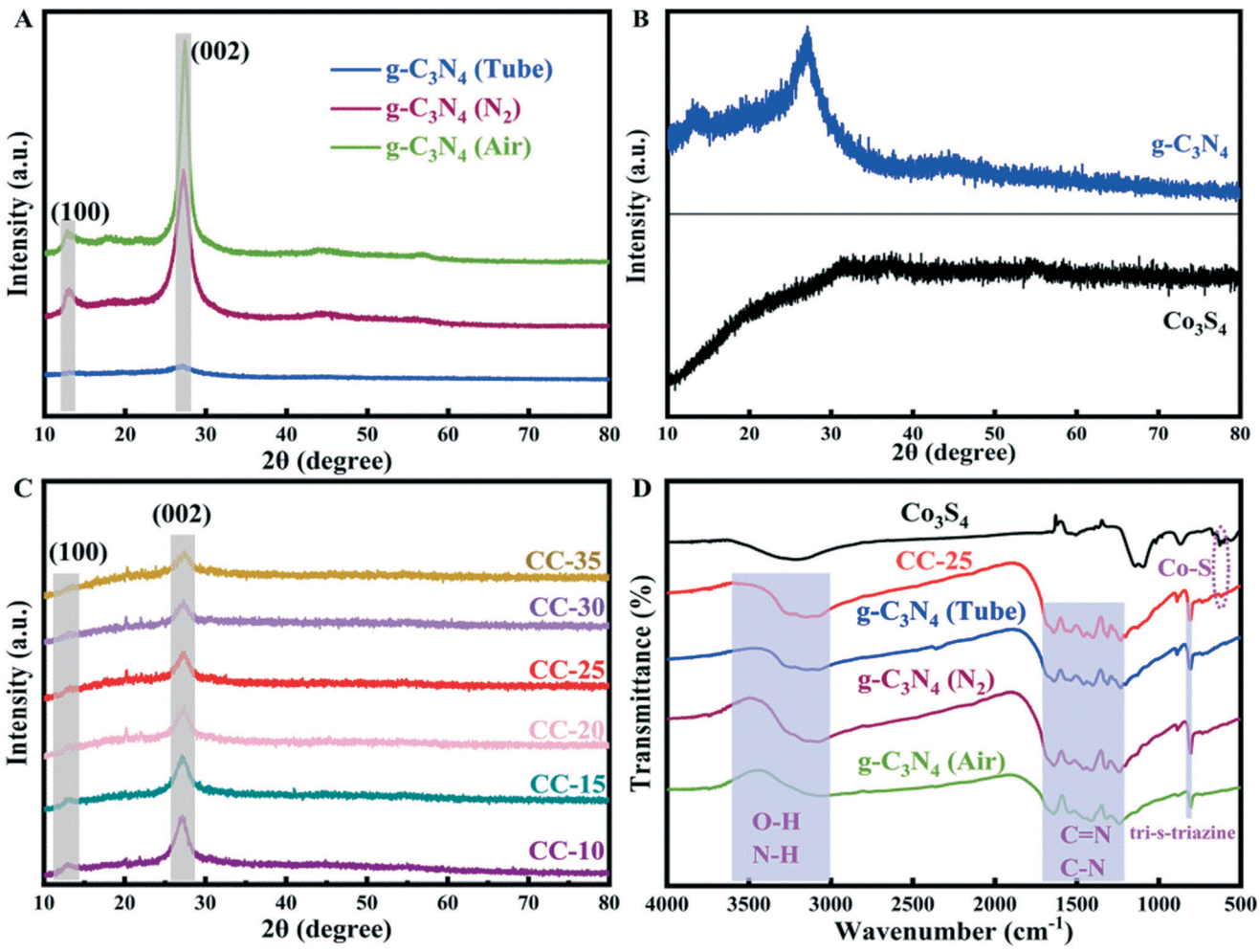

Fig. 1 XRD patterns of (A) g-C_3N_4 (prepared using different methods), (B) Co_3S_4 and g-C_3N_4 tube, (C) CC-x (x = 10, 15, 20, 25, 30, 35), and (D) FT-IR spectra of g-C_3N_4 (prepared using different methods), Co_3S_4, and CC-25.

C_3N_4 so that it becomes uneven, resulting in the same scattering/reflection effect. The scattering/reflection effect occurring on the surface of g-C_3N_4 can enhance light utilization because ultrafine Co_3S_4 nanoparticles can act as a hole in an uneven mirror to scatter and reflect light irradiating to the surface of Co_3S_4 nanoparticles, and some light can be reflected to the surface of the g-C_3N_4 tube, which is the reason for the enhanced light absorption of g-C_3N_4.

2. Results and discussion

2.1 Structural and morphological analysis

2.1.1 XRD and FTIR analysis. Fig. 1A shows XRD patterns of g-C_3N_4 synthesized using different methods, from which it can be seen that the tubular g-C_3N_4 maintains the two characteristic peaks of g-C_3N_4. The two peaks are centered at approximately 13.1° and 27.2°, as previously reported. These two peaks can be assigned to the (100) and (002), with the former one indexed to the in-plane structural packing motif, and the latter to the periodic stacking of layers along the *c*-axis.[31] The XRD pattern of Co_3S_4 presented in Fig. 1B exhibits no obvious diffraction peak due to its amorphous characteristics, which also can be confirmed by the results of HRTEM of CC-25. XRD patterns of CC-*x* (*x* = 10, 15, 20, 25, 30, 35) are shown in Fig. 1C, and no diffraction peaks of Co_3S_4 can be found in these patterns, which occurs due to the amorphous characteristics of Co_3S_4 ultrafine nanoparticles in comparison to tubular g-C_3N_4, and this can be observed from Fig. 1B.

The chemical structures of g-C_3N_4 (synthesized with different methods), Co_3S_4, and CC-25 were analyzed employing the FT-IR spectra presented in Fig. 1D. The tubular g-C_3N_4 synthesized with a two-step hydrothermal method maintained a core structure that is similar to that of bulk g-C_3N_4 (prepared in air and nitrogen). The absorption band located at approximately 807 cm^{-1} can be assigned to the tri-*s*-triazine unit,[26] which indicates a complete skeleton g-structure of g-C_3N_4. The absorption peaks located from 1200 to 1700 cm^{-1} are indexed to the C=N and C–N stretching vibration modes.[32,33] The weak absorption peaks situated in the range from 3000 to 3600 cm^{-1} are the O–H and N–H stretching vibration modes.[34] FTIR spectroscopy of Co_3S_4 shows a weak absorption peak that is centered at approximately 620 cm^{-1}, and it can be indexed to the stretching vibrations of cobalt–sulphur bonds.[35,36] In addition, the absorption peak of cobalt–sulphur bonds can

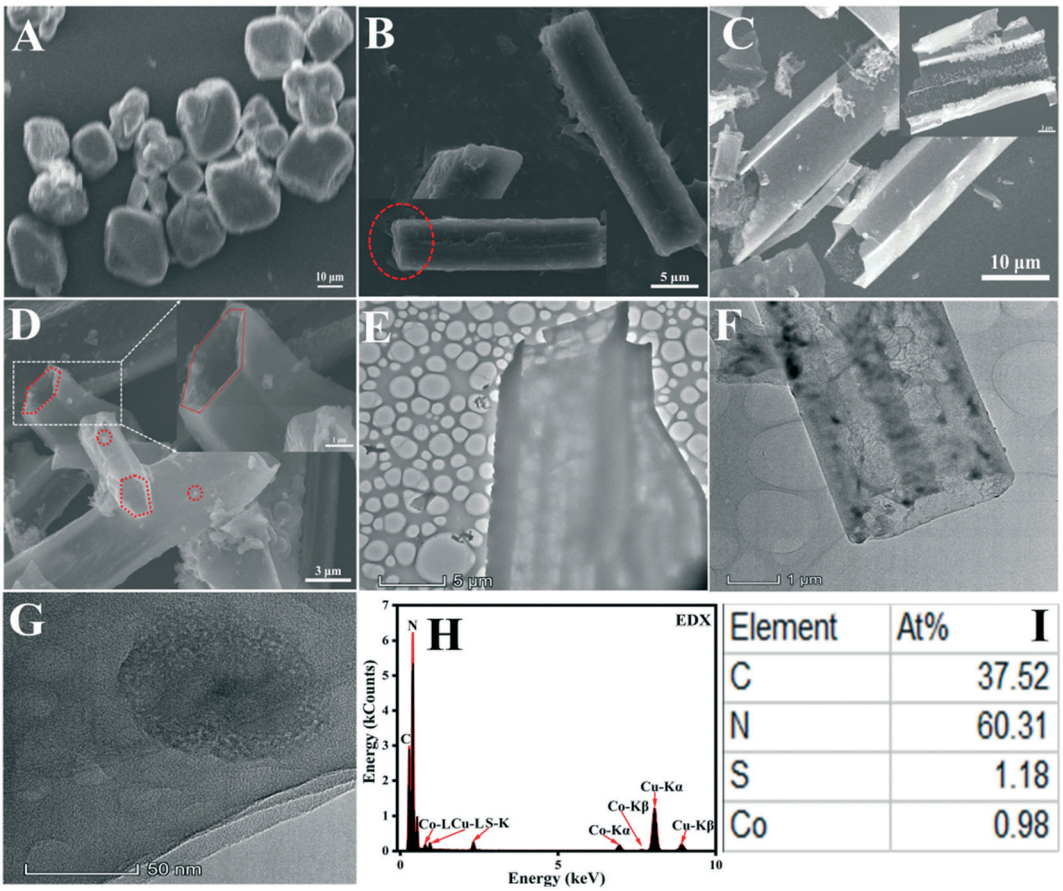

Fig. 2 SEM images of (A) melamine raw material, (B) supramolecular precursor prepared by the hydrothermal method with melamine as the raw material, (C) g-C_3N_4 tubes, (D) CC-25. TEM images of (E) g-C_3N_4 tubes and (F) CC-25. HRTEM image of (G) CC-25. (H) EDX image of CC-25. (I) The atomic fractions of C, N, S, and Co.

be found in the FTIR pattern of CC-25, which indicates that g-C_3N_4 tubes and Co_3S_4 nanoparticles were successfully combined, and this can also be proved by the EDX results.

2.1.2 SEM and TEM analysis. The SEM image shows the supramolecular precursor prepared by a hydrothermal method with melamine as raw materials. It can be seen from the SEM image of melamine (presented in Fig. 2A) without any treatment that its morphology is totally different from those of the supramolecular precursors and g-C_3N_4 tubes. Fig. 2B is an SEM image of supramolecular precursors with a hexagonal morphology but not hollow structure. When the precursors were treated in a N_2 atmosphere, the morphology changed to hexagonal tubes with weak walls. Fig. 2D displays SEM images of CC-25 with different resolution, and it can be clearly seen that g-C_3N_4 exhibits the apparent morphology of hexagonal tubes and some irregular and relatively large points assembled by ultrafine Co_3S_4 nanoparticles on the surface of these tubes. These assembled Co_3S_4 nanoparticles on the surface of g-C_3N_4 tubes can act as a mirror to reflect and scatter light incident to the surface of the tubes, which is beneficial for photocatalytic hydrogen evolution. The ultrafine Co_3S_4 nanoparticles are distributed on different surfaces of these tubes, and some are distributed on the junction of two surfaces. Co_3S_4 nanoparticles on the ridge will reflect incident light from one surface to another, and the utilization of incident light will be enhanced through this phenomenon (a schematic diagram of the scatter process is shown in Scheme S2A†). The SEM image presented in Fig. 2C and TEM image of pristine g-C_3N_4 shown in Fig. 2E illustrate its hollow structure and weak walls. The TEM images of CC-25 displayed in Fig. 2F and G show that some areas are opaque because they are occupied by many congregated ultrafine Co_3S_4 nanoparticles. As claimed in the section on H_2 evolution performance, a suitable loading amount of Co_3S_4 nanoparticles can maximally enhance the photocatalytic hydrogen performance (shown in Scheme S2B†). Most areas will be occupied when loading too many Co_3S_4 nanoparticles on the surface of g-C_3N_4 tubes, and this phenomenon will result in low utilization on surface areas because excessive Co_3S_4 nanoparticles will hinder incident light from reaching the surface of the g-C_3N_4 tubes (as shown in Scheme S2C†). The TEM DEX results (Fig. 2H) confirm the presence of elements C, N, S, and Co in CC-25. The atomic fraction (Fig. 2I) from the EDX results also reveals that the ratios of C/N and Co/S are similar to the ratios in g-C_3N_4 and Co_3S_4.

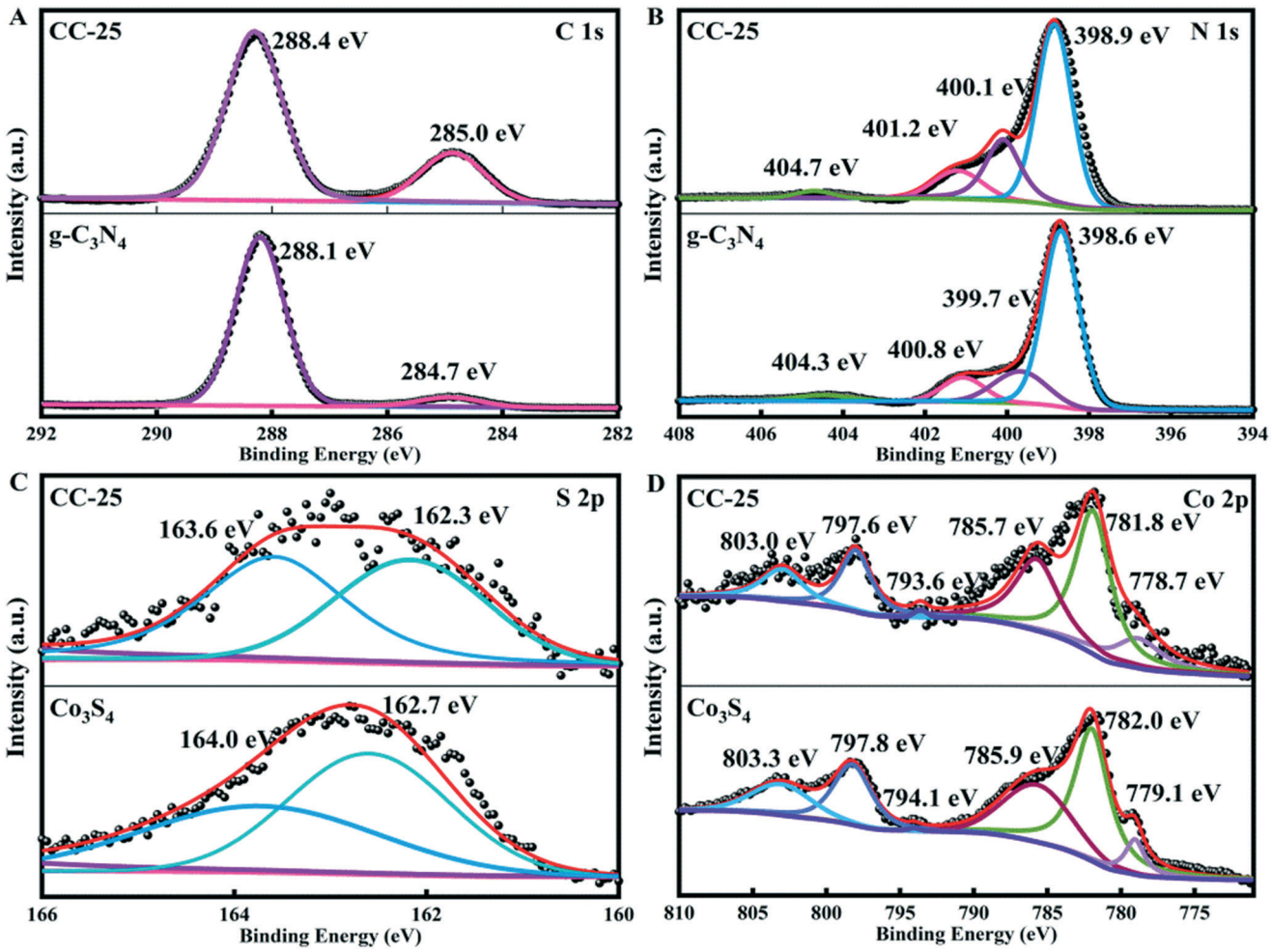

Fig. 3 High resolution XPS spectra of (A) C 1s, (B) N 1s, (C) S 2p, and (D) Co 2p.

2.1.3 XPS analysis. The transfer direction of electrons and the surface chemical valence states of elements were studied by carrying out X-ray photoelectron spectroscopy (XPS). The XPS survey spectra of g-C_3N_4, Co_3S_4, and CC-25 are presented in Fig. S1.† Fig. 3A shows the high-resolution XPS spectrum of C 1s. The two peaks with binding energies of 284.7 and 288.4 eV can be indexed to the carbon atoms in the N═C $(-N)_2$ group and the graphitic adventitious C═C/C–C bond in g-C_3N_4.[37] The high-resolution XPS spectrum of N 1s (Fig. 3B) can be deconvoluted into four peaks, and these peaks with bonding energies of 404.3, 400.8, 399.7, and 398.6 eV can be indexed to π excitation of the C═N, C–N–H, N–$(C)_3$, and C–N═C conjugated structures in g-C_3N_4, respectively.[38] There are two peaks with binding energies of 162.7 and 164.0 in the spectrum of S 2p (Fig. 3C), and the two peaks can be indexed to S (−II) in sulfide (CoS_x).[39] The high-resolution XPS spectrum of Co 2p presented in Fig. 3D contains six peaks. Those peaks with binding energies of 779.1 and 794.1 eV belong to Co $2p_{3/2}$ and Co $2p_{1/2}$, which are attributed to Co^{2+}. The peaks centered at 782.0 and 797.8 eV can be assigned to Co $2p_{3/2}$ and Co $2p_{1/2}$, and indicate the existence of Co^{3+}.[40–42] The other two peaks with binding energies of 785.9 and 803.3 eV belong to satellites.[41] In addition, the spectra of C 1s, N 1s, S 2p, and Co 2p of CC-25 were obtained, and the results are shown in Fig. 3. All binding energies of C 1s and N 1s in CC-25 shift towards higher energy, and binding energies of S 2p and Co 2p in CC-25 shift towards lower energy, which indicates that electrons are transferred from g-C_3N_4 tubes to Co_3S_4 ultrafine nanoparticles.

2.1.4 BET analysis. The pore structures of the two pristine samples and the composite were analyzed by conducting N_2 adsorption–desorption isotherms and pore size distribution analysis, as shown in Fig. 4. Fig. 4A shows that all three samples exhibited type IV isotherms with H3 hysteresis loops at the relative pressure (P/P_0) ranging from 0 to 1, which is indicative of the presence of mesopores.[15] The inset image in Fig. 4A shows that the average diameters of these samples are mainly from 2 to 50 nm, which also indicates the presence of mesopores. Fig. 4B–D illustrates the detailed adsorption–desorption isotherms and corresponding pore size distribution (inset pictures), in which the isotherms of g-

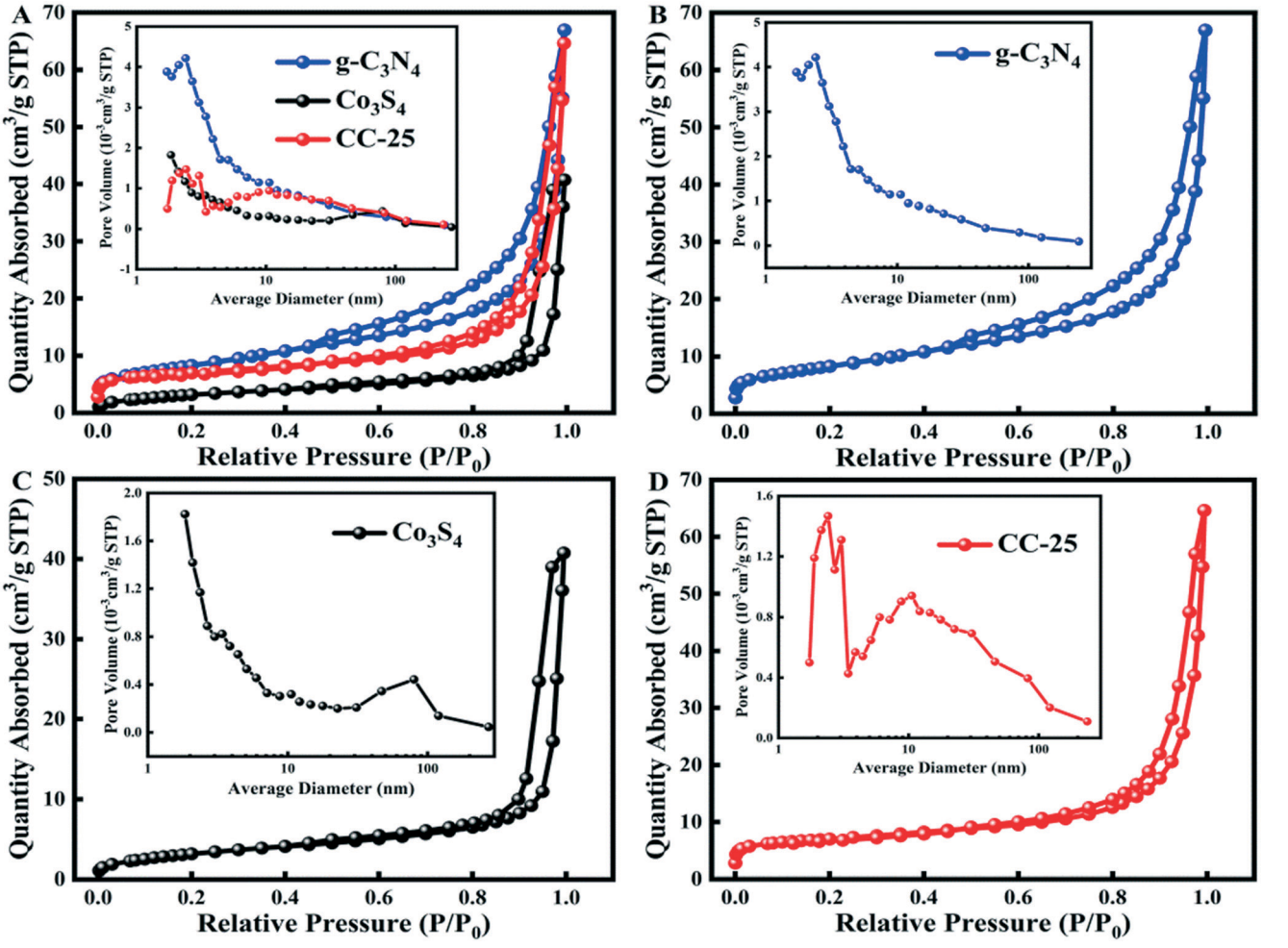

Fig. 4 (A) N_2 adsorption–desorption isotherms for g-C_3N_4 tubes, Co_3S_4, and CC-25, and corresponding pore size distribution curves (inset). (B)–(D) N_2 adsorption–desorption isotherms for g-C_3N_4 tubes, Co_3S_4, and CC-25, and corresponding pore size distribution curves (inset).

C_3N_4 tubes, Co_3S_4, and CC-25 exhibit bi-model pore size distributions, which are indicative of mesoporous structures for these samples. In addition, the hybrid exhibits the characteristics of both g-C_3N_4 tubes and Co_3S_4, demonstrating that the two materials are successfully coupled. The BET specific surface area (S_{BET}) of CC-25 (22 m^2 g^{-1}) is slightly lower than that of pristine g-C_3N_4, which indicates that the BET specific surface area is not the main factor that affects the photocatalytic H_2 evolution activity. The decrease in the S_{BET} of the composite can be attributed to many accumulated Co_3S_4 nanoparticles that occupy the surface area of the hexagonal g-C_3N_4 tubes, resulting in a decrease in the S_{BET} of CC-25. The hexagonal g-C_3N_4 tubes with a larger S_{BET} can provide a larger surface area to anchor more Co_3S_4 nanoparticles and prevent these nanoparticles from accumulating while also providing additional sites for photocatalytic reactions (Table 1).

2.2 Optical absorption properties

The photocatalytic performance is affected to some extent by the optical absorption properties of catalysts. Fig. 5A shows the optical properties of bulk g-C_3N_4 prepared by calcining melamine in air (denoted as g-C_3N_4 (air)), bulk g-C_3N_4 prepared by calcining melamine in N_2 atmosphere (denoted as g-C_3N_4 (N_2)), and tubular g-C_3N_4. The absorption edge and the absorbance of the tubular g-C_3N_4 were lower than those of the two bulk-g-C_3N_4 samples when lower than 430 nm in the visible light region. However, the absorption edge of the g-C_3N_4 tubes shifts to a longer wavelength, and the absorbance becomes stronger than that of the counterparts of bulk g-C_3N_4 (air) when the incident light is located between 430 and 521 nm. Then, the absorbance of the tubular g-C_3N_4 continues to strengthen when the incident light increases its wavelength, and eventually, it becomes the strongest among the three samples, which is indicative of the enhanced light harvesting ability of tubular g-C_3N_4 itself. The enhanced light harvesting ability of tubular g-C_3N_4 can be attributed to the multiple light scattering/reflection effect in the inner cavity of tubular g-C_3N_4 (Scheme S2A†).

The optical properties of g-C_3N_4 tubes, Co_3S_4, and CC-x (x = 10, 15, 20, 25, 30, 35) were studied using UV-vis diffuse reflectance spectra, as shown in Fig. 5B. The absorption edges of all composite samples shifted to a longer wavelength compared with the tubular g-C_3N_4, and the absorbance of these composite samples was higher than that of g-C_3N_4 tubes. The absorbance of the composite increases with an increase in the Co_3S_4 ultrafine nanoparticles loaded on the surface of g-C_3N_4 tubes. As depicted in Scheme S2B,† the ultrafine Co_3S_4 nanoparticles loaded on the surface of g-C_3N_4 tubes can act as a mirror with a rough surface to scatter and reflect the incident light. The incident light can be scattered and repeatedly reflected among the ultrafine Co_3S_4 nanoparticles. The light can also be reflected by the ultrafine Co_3S_4 nanoparticles toward different directions, and the scattered and reflected light will eventually irradiate to the surface of g-C_3N_4 tubes, which enhances the light harvesting ability of tubular g-C_3N_4, and this is the reason for the enhanced light absorbance of all composites. However, loading too many Co_3S_4 nanoparticles on the surface of g-C_3N_4 tubes will lead to a decrease in light absorbance because too many Co_3S_4 nanoparticles will hinder the incident light from irradiating to the surface of tubular g-C_3N_4 (Scheme S2C†).

Table 1 Parameters of physical adsorption

Samples	S_{BET},[a] m^2 g^{-1}	Pore volume,[b] cm^3 g^{-1}	Average pore size,[b] nm
g-C_3N_4	29	0.09	15
Co_3S_4	11	0.06	27
CC-25	22	0.09	27

[a] Obtained from the BET method. [b] Relative pressure (P/P_0) was 0.99.

2.3 Hydrogen evolution performance and stability

The photocatalytic H_2 evolution performance of g-C_3N_4, Co_3S_4, and CC-x (x = 10, 15, 20, 25, 30, 35) at pH 9 was evaluated and is shown as Fig. 6A. The photocatalytic hydrogen evolution of tubular g-C_3N_4 is 12 μmol g^{-1} h^{-1}. When the ultrafine Co_3S_4 nanoparticles are anchored on the surface of g-C_3N_4 tubes, the photocatalytic hydrogen evolution drastically increases. The photocatalytic hydrogen evolution of CC-25 is 2120 μmol g^{-1} h^{-1}, which is 176 times higher than that of pure tubular g-C_3N_4. The photocatalytic hydrogen evolution of CC-25 at different pH values was carried out, and the results are shown in Fig. 6B, from which it can be seen that the highest hydrogen evolution performance occurred at pH 9, which is indicative that it is an appropriate pH value that is suitable for hydrogen evolution. The hydrogen evolution of CC-25 decreases when the pH value is higher than 9, which likely occurs due to the decreased concentration of H^+, and thus, a decreased thermodynamic driving force for hydrogen evolution. It also was likely due to the strengthened electrostatic repulsion forces between the deprotonated EY and the negatively charged g-C_3N_4 tubes. However, lowering the pH to 8 also leads to a decrease in the hydrogen evolution of CC-25, and the H_2 evolution performance is drastically decreased when the pH value is lowered to 5. This can be explained in that an overly acidic environment will result in the protonation of triethanolamine (TEOA). Then, TEOA becomes an ineffective electron donor, and as a consequence, the H_2 evolution performance decreases. Fig. 6C shows the H_2 evolution performance of CC-25 in different sacrificial reagents, including 10% lactic acid, Na_2S/Na_2SO_3 (0.35 M/0.25 M), 15% methanol, and 15% TEOA (pH 9). The photocatalytic activity of CC-25 in 15% TEOA (pH 9) in the presence of EY is the highest and is far beyond that of other sacrificial reagents, demonstrating that the composite catalyst CC-25 is selective of sacrificial reagents, and 15% TEOA (pH 9) is the most suitable for photocatalytic H_2 evolution among these four

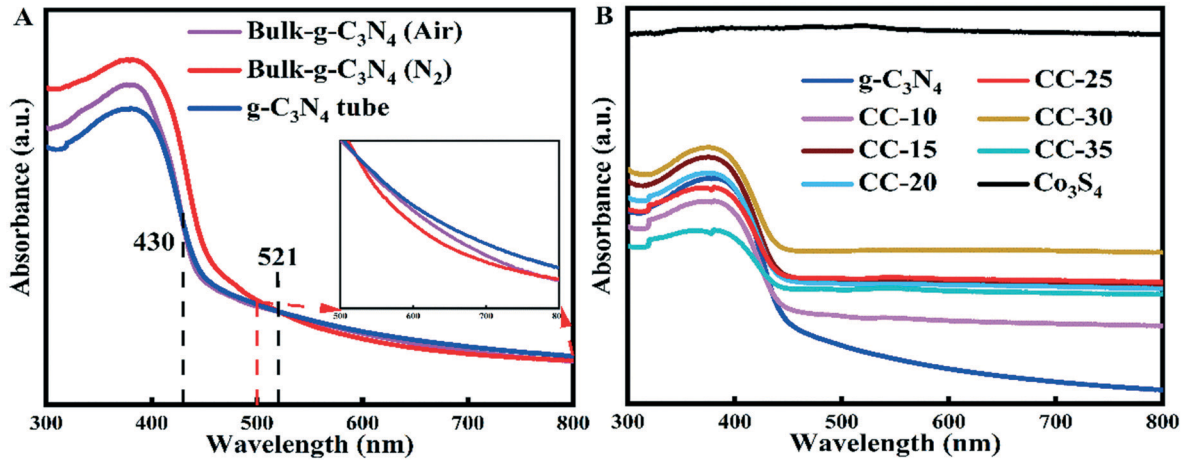

Fig. 5 UV-vis diffuse reflectance spectra of (A) g-C_3N_4 (prepared under different conditions), (B) g-C_3N_4 tubes, Co_3S_4, and CC-*x* (*x* = 10, 15, 20, 25, 30, 35).

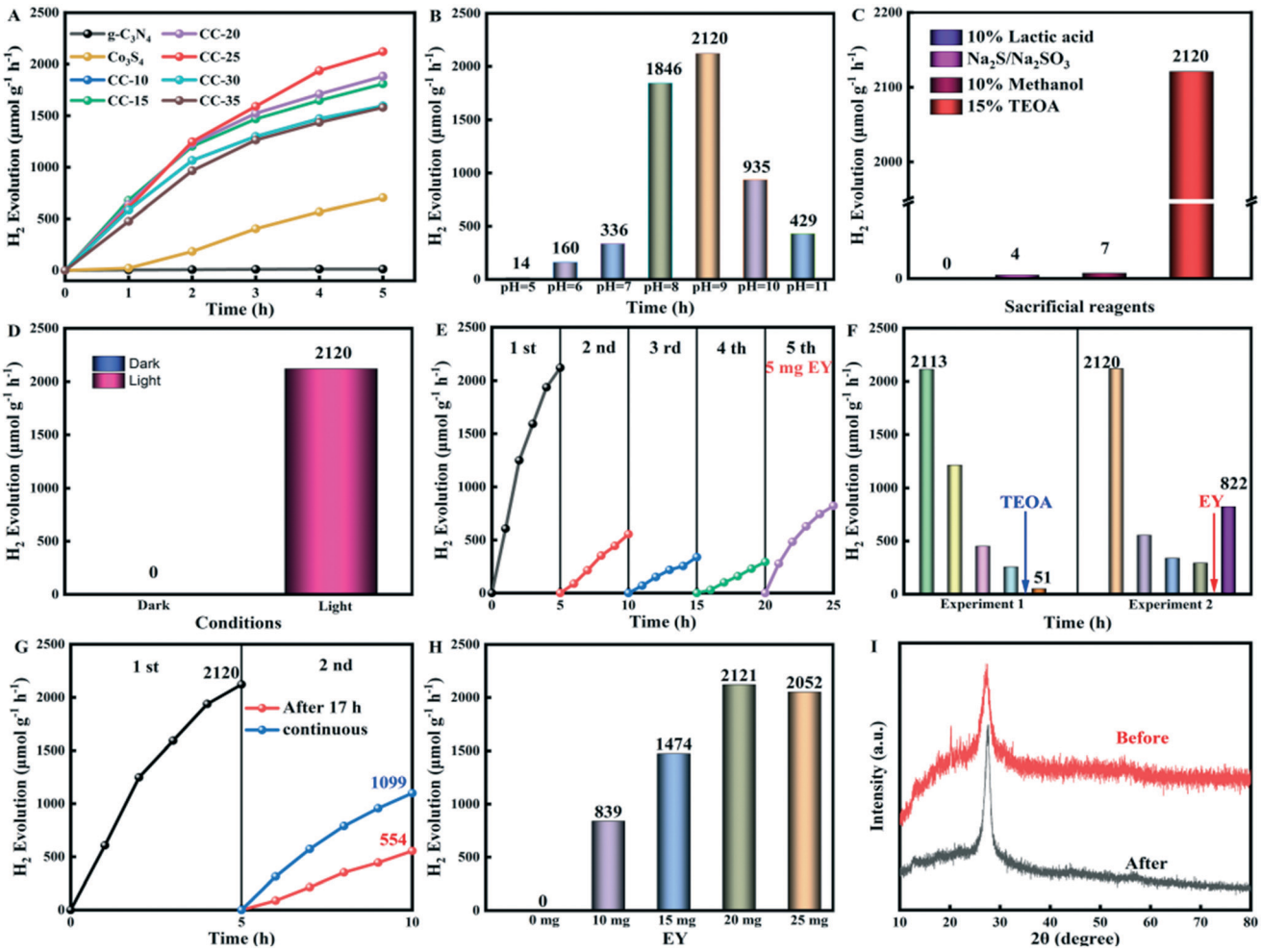

Fig. 6 (A) H_2 evolution of g-C_3N_4, Co_3S_4, and CC-10, CC-15, CC-20, CC-25, CC-30, and CC-35 within 5 h. (B) H_2 evolution of CC-25 at different pH values. (C) H_2 evolution of CC-25 in 10% lactic acid, Na_2S/Na_2SO_3 (0.35 M/0.25 M), 15% methanol, and TEOA (pH 9). (D) H_2 evolution of CC-25 under visible light and in the dark. (E) H_2 evolution stability test of CC-25. (F) Comparative experiments to study the fifth run by changing sacrificial reagents or adding EY. (G) Comparison of H_2 evolution stability test of CC-25 in the first and second runs when continuous and when 17 h apart. (H) H_2 evolution of CC-25 when adding different amounts of EY, (I) XRD patterns of CC-25 before and after the photocatalytic hydrogen evolution.

sacrificial reagents. EY was added to the system as a sensitizer to enhance the photocatalytic hydrogen evolution activity of CC-25. TEOA (15%), as the sacrificial reagent, not only can consume photogenerated holes at the valence band

of g-C_3N_4 tubes, but it also provides electrons for the transformation of EY from the triplet excited state (EY^{3}*) to the transition state ($EY^{\bullet-}$), and at last, the transition state EY can provide electrons to photocatalysts to participate in the H_2 evolution reaction. For the other three sacrificial reagents, they can act as hole consumers instead of playing the role of electron donor to provide electrons to EY for its transformation between different excited states. Therefore, the photocatalytic hydrogen evolution of CC-25 in TEOA is much higher than that in other three sacrificial reagents. The hydrogen evolution of CC-25 in the dark and under the irradiation of visible light conditions was performed and is presented in Fig. 6D. There was no H_2 produced when the lights were turned off, and it lasted for 5 h because electron–hole pairs cannot be excited.

The photocatalytic hydrogen evolution stability test of CC-25 was implemented in TEOA (pH 9) in the presence of EY, and the result is displayed in Fig. 6E. The hydrogen evolution performance of the composite catalyst was excellent in the first run, which lasted for 5 h. However, it drastically decreased when the test proceeded to the second run, and then decreased by inches in the third and the fourth runs. The drastic decrease in the second, third, and fourth runs compared with the first run can probably be attributed to two aspects. The sacrificial reagent (TEOA) in the reaction bottle was consumed because no extra TEOA was added to the reaction bottle. However, EY was degraded under the illumination of visible light in the presence of TEOA. Some extra experiments were conducted (presented in Fig. 6F) to confirm the proposed hypothesis above. In the first control experiment, the sacrificial reagent was changed in the fifth run but without adding any EY, and the hydrogen performance did not recover, but instead, continued to fall. In the second control experiment, five milligrams of EY were added to the reaction bottle in the fifth run without changing or adding the sacrificial reagent (TEOA). Then, the hydrogen evolution recovered, and it was almost 3 times higher than that of the fourth run. These results indicate that a drastic decrease in the photocatalytic hydrogen performance of CC-25 is not irrelevant to the consumption of TEOA. The hydrogen evolution performance of CC-25 in the stability test sharply decreased during the second run, which can probably be attributed to the degradation of EY under visible light because there was an interval of 17 h between the first and second runs. A control experiment was carried out to clarify what we surmised above, and the result is displayed in Fig. 6G. The hydrogen performance of CC-25 at the second run decreased almost 74% from 2120 to 554 when there was an interval of 17 h between the first and the second runs. However, the hydrogen performance of CC-25 at the second run only decreased 49% from 2120 to 1099 when the second run was carried out immediately after the first run. These results indicate that the drastic decrease in the hydrogen evolution performance of CC-25 is attributed to the degradation of EY. Also, Fig. 6I shows the XRD patterns of CC-25 before and after the photocatalytic hydrogen evolution stability tests were conducted, and there is no obvious shift in characteristic peaks, which indicates that the composite is stable. The SEM image of CC-25 after photocatalytic hydrogen evolution was implemented is shown in Fig. S4,† which also confirms the stability of the composite. Fig. 6H shows the experiment where different amounts of EY were added to the reaction system to determine the most suitable amount for photocatalytic hydrogen evolution. No H_2 can be produced when the amount of EY is 0 mg. Then, the hydrogen evolution increases with increasing amounts of added EY, but hydrogen performance decreases when excessive amounts of EY were added to the system. When the amount of EY is insufficient, it cannot provide enough electrons for the hydrogen evolution reaction. Conversely, excessive EY in the reaction system will create a shielding effect that is not beneficial for the hydrogen evolution reaction.

2.4 Transfer kinetics of charges

The transfer kinetics of photo-generated charge carriers were studied by obtaining photoluminescence (PL) and time-resolved photoluminescence (TRPL) spectra, transient photocurrent response (IT) and electrochemical impedance (EIS) spectra, and linear scan voltammetry (LSV) spectra (Fig. 7). The intensity of the fluorescence can reflect the recombination rate of the electron–hole pairs because the recombination of photo-induced electron–hole pairs will emit fluorescence, and the fluorescence can be recorded. As depicted in Fig. 7A, the EY solution (1×10^{-6} mol L^{-1}) exhibits a typical emission peak at approximately 540 nm when excited at 480 nm, being assigned to the conjugated xanthene structure with severe recombination of photogenerated electron–hole pairs. However, the emission peaks of EY-sensitized g-C_3N_4, Co_3S_4, and CC-25 exhibited a blueshift compared with pristine EY, which can be attributed to the strong interaction that occurred between EY and each pristine sample. The intensity of the emission peak decreased when tubular g-C_3N_4 was added to EY solution, and that of EY-sensitized Co_3S_4 ultrafine nanoparticles decreased to a lower status, which revealed that photogenerated electrons from EY* are easily transferred to Co_3S_4 nanoparticles. The estimated potential of EY* (−3.45 eV)[43] is more negative than that of the conduction bands of tubular g-C_3N_4 (−1.02 eV) and Co_3S_4 (−1.41 eV) ultrafine nanoparticles, which creates a difference in the energy levels, and this enables electrons to be transferred from EY to g-C_3N_4 tubes and Co_3S_4 nanoparticles. Additionally, the PL intensity of CC-25 tested in EY aqueous solution further decreased compared to pristine g-C_3N_4 after introducing Co_3S_4 ultrafine nanoparticles. This indicated that electrons from the photoexcited EY* can be separated and transferred to g-C_3N_4 tubes and Co_3S_4 nanoparticles, which resulted in PL quenching of EY. Fig. 7B shows that the photocurrent intensity of CC-25 was the lowest among the three samples, demonstrating that EY-sensitized CC-25 exhibited the lowest recombination rate of photogenerated electron–hole pairs. A more efficient transfer and separation can be obtained by introducing Co_3S_4 ultrafine

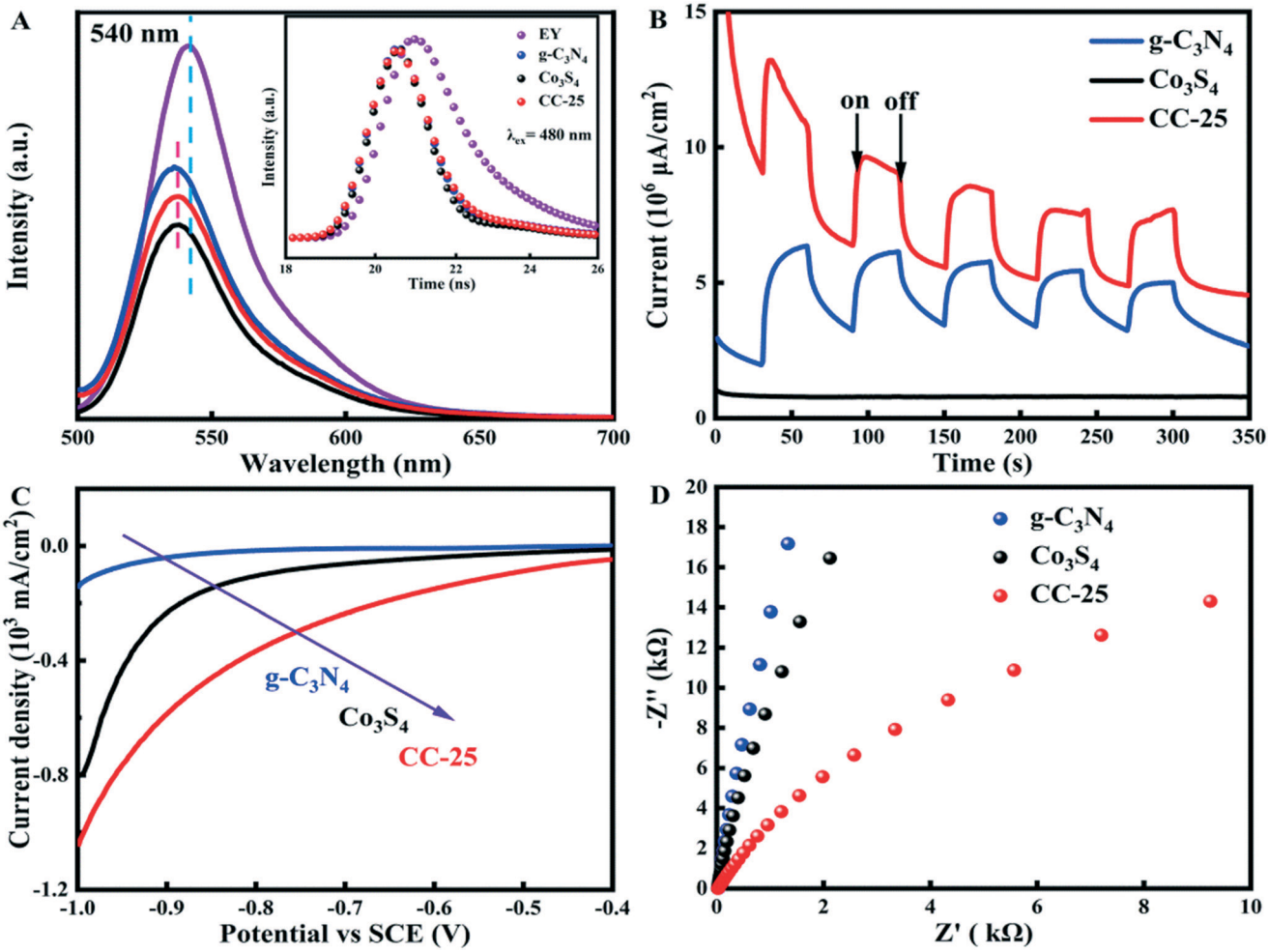

Fig. 7 (A) Photoluminescence (PL) spectroscopy of g-C_3N_4, Co_3S_4, and CC-25 (the inset image is time-resolved photoluminescence (TRPL)). (B) Photocurrent intensity of g-C_3N_4, Co_3S_4, and CC-25. (C) Linear scan voltammetry (LSV) of g-C_3N_4, Co_3S_4, and CC-25. (D) Nyquist plots of electrochemical impedance spectroscopy (EIS) of g-C_3N_4, Co_3S_4, and CC-25.

nanoparticles to form heterojunctions with tubular g-C_3N_4. The polarization curves of CC-25 (Fig. 7C) exhibited the lowest onset potential among these three samples, revealing an excellent performance in lowering the H_2-evolution overpotential. In addition, the electrochemical impedance spectroscopy (Fig. 7D) of CC-25 carried out in 0.2 M Na_2SO_4 solution showed a lower arc radius compared with those of pristine g-C_3N_4 tubes and Co_3S_4 ultrafine nanoparticles, which indicated that the introduction of Co_3S_4 accelerated the transfer and separation of electrons between these two components, thus promoting photocatalytic hydrogen evolution. The enhanced transfer and separation of photogenerated charge carriers leads to additional electrons that can be utilized in the hydrogen evolution reaction (Table 2).

2.5 Band structure

The UV-vis diffuse reflectance spectra of g-C_3N_4, Co_3S_4, and CC-25 (Fig. 8A) show that the absorption edge and absorbance of CC-25 shift toward larger wavelengths and become stronger after coupling with Co_3S_4 ultrafine nanoparticles and g-C_3N_4 tubes. Fig. 8B and C show the band gaps of g-C_3N_4 tubes and Co_3S_4 nanoparticles, and Fig. 8D shows the Mott–Schottky curves of g-C_3N_4 tubes and Co_3S_4 nanoparticles. It is well known that the conduction band of an n-type semiconductor is more negative by approximately −0.2 or −0.1 eV than its flat band.[44,45] Hence, the conduction bands of g-C_3N_4 and Co_3S_4 were calculated to be −1.26 and −1.65 V *vs.* SCE (saturate calomel electrode), and the conduction bands of these two components can also be presented as −1.02 and −1.41 V *vs.* NHE (normal hydrogen

Table 2 Parameters of emission decay of EY, g-C_3N_4, Co_3S_4, and CC-25

Samples	τ_1,[a] ns	τ_2, ns	τ_{av}, ns	χ^2
EY	0.99 (B_1: 64.27%)	1.78 (B_1: 35.73%)	1.17	1.31
g-C_3N_4	0.43 (B_1[b]: 91.37%)	4.92 (B_2: 8.63%)	0.47	1.48
Co_3S_4	4.42 (B_1: 5.19%)	0.32 (B_2: 94.81%)	0.33	1.45
CC-25	0.49 (B_1: 93.76%)	4.77 (B_2: 6.24%)	0.53	1.46

[a] τ: Lifetime. [b] B: pre-exponential factor.

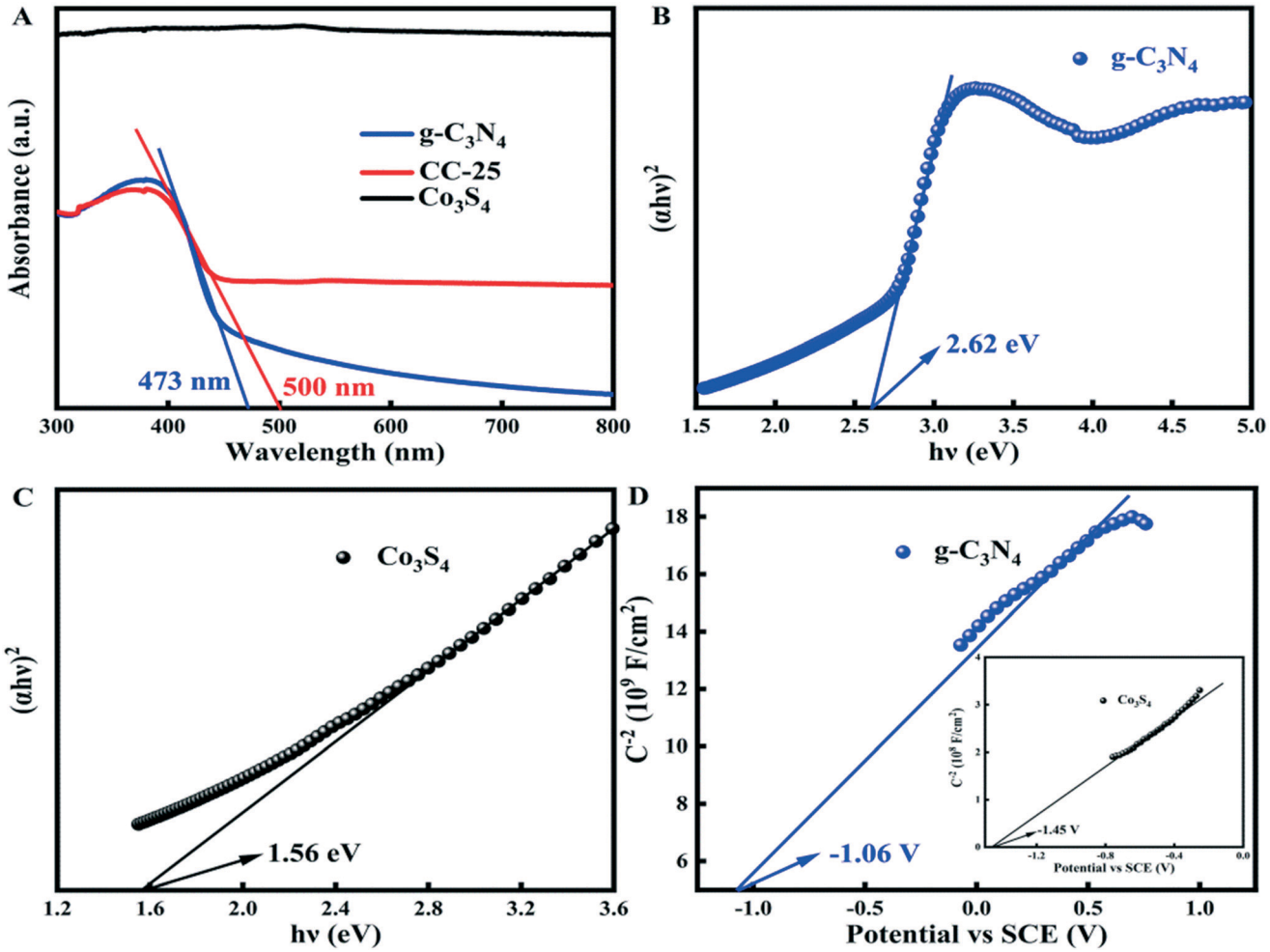

Fig. 8 (A) UV-vis diffuse reflectance spectra of g-C_3N_4, Co_3S_4, and CC-25. The corresponding plots of $(\alpha h\nu)^2$ *versus* $h\nu$ of (B) g-C_3N_4 tubes and (C) Co_3S_4. (D) Mott–Schottky curves of g-C_3N_4 and Co_3S_4 (inset curve).

electrode) ($E_{NHE} = E_{SCE} + 0.241$ V).[46–48] In addition, the valance band of g-C_3N_4 and Co_3S_4 was determined to be 1.6 and 0.15 V by the equation: $E_{VB} = E_{CB} + E_g$.

2.6 Reaction mechanism

The light-harvesting performance of tubular g-C_3N_4 can be enhanced through the multiple scatter/reflection effect that occurs in the inner cavity of g-C_3N_4. Additionally, the amorphous Co_3S_4 ultrafine nanoparticles anchored on the outside surface of g-C_3N_4 tubes can act as a mirror to scatter and reflect light, thus enhancing the light-harvesting performance of the composite catalyst. A possible mechanism for the photocatalytic hydrogen evolution is proposed (Fig. 9) to more optimally understand the entire process of photocatalysis based on all the results discussed in the above sections. Singlet excited states of EY^{1}* can be produced after absorbing light by EY, and then, the singlet excited states will produce triplet excited states EY^{3}* through fast intersystem crossing (ISC).[49] The triplet excited states EY^{3}* are reductively quenched when TEOA is added to the system, producing $EY^{\bullet-}$. Electrons from $EY^{\bullet-}$ can be transferred to the conduction bands of the Co_3S_4 ultrafine nanoparticles and g-C_3N_4 tubes, and at the same time, parts

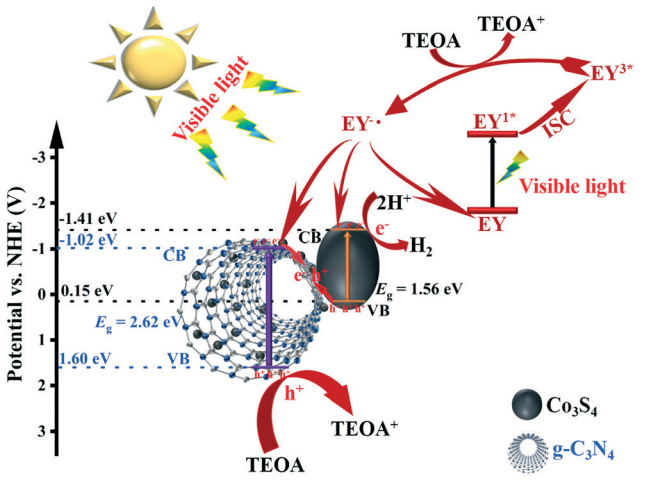

Fig. 9 Proposed mechanism for enhanced photocatalytic H_2 evolution under visible light irradiation.

of $EY^{\bullet-}$ return to the ground state. Additionally, g-C_3N_4 itself can be excited by absorbing light with energy that exceeds its band gap. Then, electron–hole pairs are excited, and electrons are later transferred to the conduction band (CB) of g-C_3N_4 tubes. Co_3S_4 ultra-fine nanoparticles can also be excited by visible light in a process similar to that which g-C_3N_4 tubes undergo. Electrons from the CB of g-C_3N_4 tubes and holes from the valence band (VB) of Co_3S_4 ultrafine nanoparticles recombine in the interface after these two semiconductors are excited by visible light, and through this, the recombination rate of electron–hole pairs in both of the materials is reduced. The solid–solid contact between these two materials forms a "Step-scheme" transfer route between them, in which electrons from the CB of g-C_3N_4 and holes from the VB of Co_3S_4 recombine in their interface. For g-C_3N_4 tubes, electrons are excited and transferred to its CB, and then subsequently transferred to the VB of Co_3S_4 to recombine with photoexcited holes. For Co_3S_4, photoexcited holes are consumed by electrons from the CB of g-C_3N_4, and electrons are transferred to the CB where H_2 is produced.

3. Conclusion

In summary, we successfully synthesized a heterojunction composed of ultrafine Co_3S_4 nanoparticles on g-C_3N_4 tubes. The light harvesting of g-C_3N_4 was enhanced due to the scatter and reflect effect in the inner cavity of the g-C_3N_4 tubes. The introduced Co_3S_4 ultrafine nanoparticles act as a mirror to repeatedly scatter and reflect incident light, which enhances light utilization. The composite catalyst performed a photocatalytic hydrogen evolution activity that was significantly improved (176 times) compared with pristine g-C_3N_4 tubes in the visible light region. Such a significant improvement in the performance of photocatalytic H_2 production can be attributed to the formation of a step-scheme heterojunction between the two materials. This work will provide guidance for studying the step-scheme photocatalysts.

Author contributions

Yuanpeng Wang and Xuqiang Hao designed the experiments, Zhiliang Jin and Tiansheng Zhao contributed reagents/materials and analysis tools, and Yuanpeng Wang and Lijun Zhang wrote the paper.

Conflicts of interest

The authors declare that they have no conflicts of interest.

Acknowledgements

This work was financially supported by the Natural Science Foundation of the Ningxia Hui Autonomous Region (2020AAC03204 and 2020AAC03208 and 2020AAC02026), the Open Project of State Key Laboratory of High-efficiency Utilization of Coal and Green Chemical Engineering, Ningxia University (2019-KF-36).

References

1 L. Yin, S. Wang, C. Yang, S. Lyu and X. Wang, Modulation of Polymeric Carbon Nitrides through Supramolecular Preorganization for Efficient Photocatalytic Hydrogen Generation, *ChemSusChem*, 2019, **12**, 3320–3325.
2 J. Fu, Q. Xu, J. Low, C. Jiang and J. Yu, Ultrathin 2D/2D WO_3/g-C_3N_4 step-scheme H_2-production photocatalyst, *Appl. Catal., B*, 2019, **243**, 556–565.
3 X. Meng, C. Zhang, C. Dong, W. Sun, D. Ji and Y. Ding, Carbon quantum dots assisted strategy to synthesize Co@NC for boosting photocatalytic hydrogen evolution performance of CdS, *Chem. Eng. J.*, 2020, **389**, 124432.
4 M. Zhang, Q. Hu, K. Ma, Y. Ding and C. Li, Pyroelectric effect in CdS nanorods decorated with a molecular Co-catalyst for hydrogen evolution, *Nano Energy*, 2020, **73**, 104810.
5 H. Gong, Z. Li, Z. Chen, Q. Liu, M. Song and C. Huang, NiSe/$Cd_{0.5}Zn_{0.5}S$ Composite Nanoparticles for Use in p–n Heterojunction-Based Photocatalysts for Solar Energy Harvesting, *ACS Appl. Nano Mater.*, 2020, **3**, 3665–3674.
6 Z. Chen, H. Gong, Q. Liu, M. Song and C. Huang, $NiSe_2$ Nanoparticles Grown in Situ on CdS Nanorods for Enhanced Photocatalytic Hydrogen Evolution, *ACS Sustainable Chem. Eng.*, 2019, **7**, 16720–16728.
7 Y. Li, H. Li, Y. Li, S. Peng and Y. H. Hu, Fe-B alloy coupled with Fe clusters as an efficient cocatalyst for photocatalytic hydrogen evolution, *Chem. Eng. J.*, 2018, **344**, 506–513.
8 Y. Li, Z. Jin, L. Zhang and K. Fan, Controllable design of Zn-Ni-P on g-C_3N_4 for efficient photocatalytic hydrogen production, *Chin. J. Catal.*, 2019, **40**, 390–402.
9 T. Jia, F. Fu, J. Li, Z. Deng, F. Long, D. Yu, Q. Cui and W. Wang, Rational construction of direct Z-scheme SnS/g-C_3N_4 hybrid photocatalyst for significant enhancement of visible-light photocatalytic activity, *Appl. Surf. Sci.*, 2020, **499**, 143941.
10 T. Jia, F. Fu, D. Yu, J. Cao and G. Sun, Facile synthesis and characterization of N-doped TiO_2/C nanocomposites with enhanced visible-light photocatalytic performance, *Appl. Surf. Sci.*, 2018, **430**, 438–447.
11 T. Jia, F. Fu, J. Li, W. Wang and X. Hu, Constructing a novel Zn_2SnO_4/C/AgBr nanocomposite with extended spectral response and improved photocatalytic performance, *J. Alloys Compd.*, 2019, **783**, 687–696.
12 L. Su, L. Luo, H. Song, Z. Wu, W. Tu, Z.-j. Wang and J. Ye, Hemispherical shell-thin lamellar WS_2 porous structures composited with CdS photocatalysts for enhanced H_2 evolution, *Chem. Eng. J.*, 2020, **388**, 124346.
13 F. Yang, D. Liu, Y. Li, L. Cheng and J. Ye, Lithium incorporation assisted synthesis of ultra-small Mo_2C nanodots as efficient photocatalytic H_2 evolution cocatalysts, *Chem. Eng. J.*, 2020, **399**, 125794.
14 H. Lin, K. Zhang, G. Yang, Y. Li, X. Liu, K. Chang, Y. Xuan and J. Ye, Ultrafine nano 1T-MoS_2 monolayers with NiOx as dual co-catalysts over TiO_2 photoharvester for efficient photocatalytic hydrogen evolution, *Appl. Catal., B*, 2020, **279**, 119387.

15 Q. Xu, B. Zhu, B. Cheng, J. Yu, M. Zhou and W. Ho, Photocatalytic H_2 evolution on graphdiyne/g-C_3N_4 hybrid nanocomposites, *Appl. Catal., B*, 2019, **255**, 117770.
16 Z. Jin, L. Zhang, G. Wang, Y. Li and Y. Wang, Graphdiyne formed a novel CuI-GD/g-C_3N_4 S-scheme heterojunction composite for efficient photocatalytic hydrogen evolution, *Sustainable Energy Fuels*, 2020, **4**, 5088–5101.
17 Y. Li, H. Yang, G. Wang, B. Ma and Z. Jin, Distinctive Improved Synthesis and Application Extensions Graphdiyne for Efficient Photocatalytic Hydrogen Evolution, *ChemCatChem*, 2020, **12**, 1985–1995.
18 X. Li, J. Xiong, X. Gao, J. Ma, Z. Chen, B. Kang, J. Liu, H. Li, Z. Feng and J. Huang, Novel BP/BiOBr S-scheme nano-heterojunction for enhanced visible-light photocatalytic tetracycline removal and oxygen evolution activity, *J. Hazard. Mater.*, 2020, **387**, 121690.
19 X. Wang, K. Maeda, A. Thomas, K. Takanabe, G. Xin, J. M. Carlsson, K. Domen and M. Antonietti, A metal-free polymeric photocatalyst for hydrogen production from water under visible light, *Nat. Mater.*, 2008, **8**, 76–80.
20 H. Wang, X. Li and J. Yang, The g-C_3N_4/C_2N Nanocomposite: A g-C_3N_4-Based Water-Splitting Photocatalyst with Enhanced Energy Efficiency, *ChemPhysChem*, 2016, **17**, 2100–2104.
21 Z. Zeng, H. Yu, X. Quan, S. Chen and S. Zhang, Structuring phase junction between tri-s-triazine and triazine crystalline C_3N_4 for efficient photocatalytic hydrogen evolution, *Appl. Catal., B*, 2018, **227**, 153–160.
22 Z. You, Y. Su, Y. Yu, H. Wang, T. Qin, F. Zhang, Q. Shen and H. Yang, Preparation of g-C_3N_4 nanorod/$InVO_4$ hollow sphere composite with enhanced visible-light photocatalytic activities, *Appl. Catal., B*, 2017, **213**, 127–135.
23 Q. Han, B. Wang, Y. Zhao, C. Hu and L. Qu, A Graphitic-C_3N_4 "Seaweed" Architecture for Enhanced Hydrogen Evolution, *Angew. Chem., Int. Ed.*, 2015, **54**, 11433–11437.
24 Y. Li, R. Jin, Y. Xing, J. Li, S. Song, X. Liu, M. Li and R. Jin, Macroscopic Foam-Like Holey Ultrathin g-C_3N_4 Nanosheets for Drastic Improvement of Visible-Light Photocatalytic Activity, *Adv. Energy Mater.*, 2016, **6**, 1601273.
25 Y. Li, M. Gu, T. Shi, W. Cui, X. Zhang, F. Dong, J. Cheng, J. Fan and K. Lv, Carbon vacancy in C_3N_4 nanotube: Electronic structure, photocatalysis mechanism and highly enhanced activity, *Appl. Catal., B*, 2020, **262**, 118281.
26 S. Wan, M. Ou, Y. Wang, Y. Zeng, Y. Xiong, F. Song, J. Ding, W. Cai, S. Zhang and Q. Zhong, Protonic acid-assisted universal synthesis of defect abundant multifunction carbon nitride semiconductor for highly-efficient visible light photocatalytic applications, *Appl. Catal., B*, 2019, **258**, 118011.
27 D. Long, W. Chen, S. Zheng, X. Rao and Y. Zhang, Barium- and Phosphorus-Codoped g-C_3N_4 Microtubes with Efficient Photocatalytic H_2 Evolution under Visible Light Irradiation, *Ind. Eng. Chem. Res.*, 2020, **59**, 4549–4556.
28 Y. Hong, L. Wang, E. Liu, J. Chen, Z. Wang, S. Zhang, X. Lin, X. Duan and J. Shi, A curly architectured graphitic carbon nitride (g-C_3N_4) towards efficient visible-light photocatalytic H_2 evolution, *Inorg. Chem. Front.*, 2020, **7**, 347–355.
29 N. A. Wasio, R. C. Quardokus, R. P. Forrest, C. S. Lent, S. A. Corcelli, J. A. Christie, K. W. Henderson and S. A. Kandel, Self-assembly of hydrogen-bonded two-dimensional quasicrystals, *Nature*, 2014, **507**, 86–89.
30 T. Jordan, N. Fechler, J. Xu, T. J. K. Brenner, M. Antonietti and M. Shalom, "Caffeine Doping" of Carbon/Nitrogen-Based Organic Catalysts: Caffeine as a Supramolecular Edge Modifier for the Synthesis of Photoactive Carbon Nitride Tubes, *ChemCatChem*, 2015, **7**, 2826–2830.
31 J. Zhang, X. Chen, K. Takanabe, K. Maeda, K. Domen, J. D. Epping, X. Fu, M. Antonietti and X. Wang, Synthesis of a Carbon Nitride Structure for Visible-Light Catalysis by Copolymerization, *Angew. Chem., Int. Ed.*, 2010, **49**, 441–444.
32 H. Ye, Z. Wang, F. Yu, S. Zhang, K. Kong, X. Gong, J. Hua and H. Tian, Fluorinated conjugated poly(benzotriazole)/g-C_3N_4 heterojunctions for significantly enhancing photocatalytic H_2 evolution, *Appl. Catal., B*, 2020, **267**, 118577.
33 Y. Chen, F. Su, H. Xie, R. Wang, C. Ding, J. Huang, Y. Xu and L. Ye, One-step construction of S-scheme heterojunctions of N-doped MoS_2 and S-doped g-C_3N_4 for enhanced photocatalytic hydrogen evolution, *Chem. Eng. J.*, 2021, **404**, 126498.
34 M. Wu, J. Zhang, B.-b. He, H.-w. Wang, R. Wang and Y.-s. Gong, In-situ construction of coral-like porous P-doped g-C_3N_4 tubes with hybrid 1D/2D architecture and high efficient photocatalytic hydrogen evolution, *Appl. Catal., B*, 2019, **241**, 159–166.
35 W. Li, Y. Li, C. Yang, Q. Ma, K. Tao and L. Han, Fabrication of 2D/2D nanosheet heterostructures of ZIF-derived Co_3S_4 and g-C_3N_4 for asymmetric supercapacitors with superior cycling stability, *Dalton Trans.*, 2020, **49**, 14017–14029.
36 V. Shrivastav, S. Sundriyal, P. Goel, V. Shrivastav, U. K. Tiwari and A. Deep, ZIF-67 derived Co_3S_4 hollow microspheres and WS_2 nanorods as a hybrid electrode material for flexible 2V solid-state supercapacitor, *Electrochim. Acta*, 2020, **345**, 136194.
37 Z. Liang, S. Yang, X. Wang, H. Cui, X. Wang and J. Tian, The metallic 1T-phase WS_2 nanosheets as cocatalysts for enhancing the photocatalytic hydrogen evolution of g-C_3N_4 nanotubes, *Appl. Catal., B*, 2020, **274**, 119114.
38 X. Han, D. Xu, L. An, C. Hou, Y. Li, Q. Zhang and H. Wang, Ni-Mo nanoparticles as co-catalyst for drastically enhanced photocatalytic hydrogen production activity over g-C_3N_4, *Appl. Catal., B*, 2019, **243**, 136–144.
39 J. Fu, C. Bie, B. Cheng, C. Jiang and J. Yu, Hollow CoSx Polyhedrons Act as High-Efficiency Cocatalyst for Enhancing the Photocatalytic Hydrogen Generation of g-C_3N_4, *ACS Sustainable Chem. Eng.*, 2018, **6**, 2767–2779.
40 C. Liang, X. Zhang, P. Feng, H. Chai and Y. Huang, ZIF-67 derived hollow cobalt sulfide as superior adsorbent for effective adsorption removal of ciprofloxacin antibiotics, *Chem. Eng. J.*, 2018, **344**, 95–104.
41 H. Yang, J. Yin, R. Cao, P. Sun, S. Zhang and X. Xu, Constructing highly dispersed 0D Co_3S_4 quantum dots/2D g-C_3N_4 nanosheets nanocomposites for excellent photocatalytic performance, *Sci. Bull.*, 2019, **64**, 1510–1517.

42 Y. Du, X. Zhu, X. Zhou, L. Hu, Z. Dai and J. Bao, Co_3S_4 porous nanosheets embedded in graphene sheets as high-performance anode materials for lithium and sodium storage, *J. Mater. Chem. A*, 2015, **3**, 6787–6791.

43 S. Min and G. Lu, Enhanced Electron Transfer from the Excited Eosin Y to mpg-C_3N_4 for Highly Efficient Hydrogen Evolution under 550 nm Irradiation, *J. Phys. Chem. C*, 2012, **116**, 19644–19652.

44 Y. Wang, X. Hao, L. Zhang, Y. Li and Z. Jin, Rational Design of All-Solid-State 0D/2D $Mn_{0.2}Cd_{0.8}S/CeO_2$ Direct Z-Scheme for Photocatalytic Hydrogen Evolution, *Energy Fuels*, 2020, **34**, 2599–2611.

45 L. Zhang, X. Hao, Y. Wang, Z. Jin and Q. Ma, Construction strategy of Mo-S@Mo-P heterojunction formed with in-situ phosphating Mo-S nanospheres toward efficient photocatalytic hydrogen production, *Chem. Eng. J.*, 2020, **391**, 123545.

46 Y. Wang, G. Wang, L. Zhang, Z. Jin and T. Zhao, Hydroxides $Ni(OH)_2$&$Ce(OH)_3$ as a novel hole storage layer for enhanced photocatalytic hydrogen evolution, *Dalton Trans.*, 2019, **48**, 17660–17672.

47 X. Hao, J. Zhou, Z. Cui, Y. Wang, Y. Wang and Z. Zou, Zn-vacancy mediated electron-hole separation in ZnS/g-C_3N_4 heterojunction for efficient visible-light photocatalytic hydrogen production, *Appl. Catal., B*, 2018, **229**, 41–51.

48 H. Liu, T. Yan, Z. Jin and Q. Ma, CoP nanoparticles as cocatalyst modified the CdS/$NiWO_4$ p–n heterojunction to produce hydrogen efficiently, *New J. Chem.*, 2020, **44**, 1426–1438.

49 L. Yang, J. Huang, L. Shi, L. Cao, W. Zhou, K. Chang, X. Meng, G. Liu, Y. Jie and J. Ye, Efficient hydrogen evolution over Sb doped SnO_2 photocatalyst sensitized by Eosin Y under visible light irradiation, *Nano Energy*, 2017, **36**, 331–340.